Supporting Information for: Conduction band replicas in a 2D moiré semiconductor heterobilayer

Abigail J. Graham[1], Heonjoon Park[2], Paul V. Nguyen[2], James Nunn[1], Viktor Kandyba[3], Mattia Cattelan[3], Alessio Giampietri[3], Alexei Barinov[3], Kenji Watanabe[4], Takashi Taniguchi[5], Anton Andreev[2], Mark Rudner[2], Xiaodong Xu[2,6], Neil R. Wilson[1] & David H. Cobden[2]

[1] Department of Physics, University of Warwick, Coventry, CV4 7AL, U.K.

[2] Department of Physics, University of Washington, Seattle, WA, USA.

[3] Elettra – Sincrotrone Trieste, S.C.p.A, Basovizza (TS), 34149, Italy.

[4] Research Center for Electronic and Optical Materials, National Institute for Materials Science, 1-1 Namiki, Tsukuba 305-0044, Japan

[5] Research Center for Materials Nanoarchitectonics, National Institute for Materials Science, 1-1 Namiki, Tsukuba 305-0044, Japan.

[6] Department of Materials Science and Engineering, University of Washington, Seattle, WA, USA.

Section 1: Methods 2

Section 2: Piezo-force microscopy phase images for device 1 (6° twisted WS_2/WSe_2) 3

Section 3: Photoluminescence and reflectance measurements to confirm twist angle 3

Section 4: Optical, SPEM and SPIM images at multiple gate voltages 4

Section 5: Comparison of monolayer and heterobilayer band alignments and band broadening 5

Section 6: Twist angle dependence of WS_2/WSe_2 band structure 6

Section 7: μARPES of WSe_2 on WS_2. 7

Section 8: Graphene Dirac cone replicas for $WS_2/MoSe_2$ heterobilayer 7

Section 9: WS_2/WSe_2 heterobilayer with 9° twist angle 8

Section 10: Search for valence band replicas in 2° heterobilayer 9

Section 11: Moiré replica intensities at 2° and 6° twist angle. 9

Section 12: Perturbation theory for the modification of the Bloch states by the moiré potential 10

Section 13: Determining band shifts, carrier concentrations, photocurrent, and the conduction band minimum 12

Section 1: Methods

Sample Fabrication

Standard heated exfoliation and polycarbonate (PC) film-based dry transfer[1] were used. hBN flakes no thicker than 15 nm were chosen to optimize gating efficiency, which under ARPES excitation is negatively impacted by photoexcited carriers in the hBN generating a current to the gate electrode. The Pt/Ti (30nm/5nm) electrodes were predefined using electron-beam lithography. The smaller electrode contacts the graphite gate, as indicated in the optical micrograph in Fig. 1c (see Fig. S3) The larger electrode, which contacts the graphene, is grounded and covers most of the chip to minimize electrostatic distortion of the photoelectron spectrum when applying a gate voltage. The edge of the graphene was patterned into a comb shape because much stronger CB photoemission is obtained from the exposed WSe_2/WS_2 heterobilayer between the comb teeth.

All heterostructures are built in three separate parts. First the hBN/graphite back gate is stacked and deposited onto the substrate with electrodes. Then the WSe_2 and WS_2 are stacked then transferred onto the gate. Finally, the patterned graphene is picked up and transferred onto the rest of the structure. Following each step, the new surface of the substrate or stack is cleaned using contact-mode AFM (Bruker Dimension Icon with OTESPA-R3 cantilevers, setpoint 0.1 V, and line spacing 10 nm/line), with a low velocity (usually 2 µm/s) when cleaning monolayers to minimize tearing. The sample substrates are mounted in dual-inline packages using ultra-high vacuum, high-temperature compatible silver epoxy and wire-bonded. Bare wire is wrapped around the package pins, fixed with epoxy, and are mechanically clamped to leads on the sample mount.

µARPES with in-situ electrostatic gating

µARPES measurements with in-situ electrostatic gating were conducted at the Spectromicroscopy beamline at Elettra synchrotron[2]. Linearly polarised light was incident on the sample at 45° to the surface normal with a photon energy of 27 eV. The beam was focused to a submicron spot-size on the sample using a Schwarzchild objective. Photoemitted electrons from the top few layers of the sample were collected by an internal moveable hemispherical electron analyser. Under the measurement conditions, the energy and momentum resolution of the 2D detector were roughly 50 meV and 0.03 $Å^{-1}$, respectively. Devices were mounted on sample plates with electrical contacts and annealed at 300 – 350 °C for around 12 hours before measurements. A long anneal time and high temperature were required due to the large size of the chip carrier and sample plate used for in-situ gating. Scanned photoemission microscopy (SPEM) and scanned photocurrent microscopy (SPIM) combined with optical images were used to locate the region of interest on the sample. Energy-momentum slices were obtained by interpolating multiple closely spaced detector images taken along the high symmetry directions of the Brillouin zone. Constant energy maps were extracted from three-dimensional data sets, $I(E, k_x, k_y)$. The

Determining carrier concentrations and EF

The capacitance to the back gate was calculated using $C = \varepsilon_0 \varepsilon_{\mathrm{hBN}} / d_{\mathrm{hBN}}$, where $\varepsilon_{\mathrm{hBN}}$ = 4.5 and the thickness of the hBN was $d_{\mathrm{hBN}} = 8.3$ nm (6° sample) or 9.0 nm (2° sample). From the capacitance and electrostatic shift of the electronic bands, ΔE_Γ, at each gate voltage V_g, the carrier concentration was found from $n_\mathrm{g} = C(V_\mathrm{g} - \Delta E_\Gamma)/e$. Band shifts, carrier concentrations and photocurrent against gate voltage are displayed in SI Sec. 11 for the 6° twist angle sample. The carrier concentration was then used to find the position of the CB edge, E_c, relative to E_F using $n = \int_{E_c}^{\infty} g_c \frac{1}{1+e^{(E-E_\mathrm{F})/k_\mathrm{B}T}} dE$, where $g_\mathrm{c} = \frac{g_S g_v m_e^*}{\pi \hbar^2}$ is the density of states of the populated 2D parabolic bands. For the WS_2 conduction bands at **K**, the values used were $g_s = 2$, $g_v = 2$, $m_e^* = 0.27\ \mathrm{m}_0$[37] and a splitting of 29 meV[39]. For the WS_2 conduction band at **Q**, the values used were $g_s = 1$, $g_v = 6$, $m_e^* = 0.70 m_0$

(average of the two monolayer values[37]) and an energy difference between $\mathbf{Q}$ and the CBM of 7.1 ± 0.8 meV found from the change in chemical potential between +1.85 V (lowest voltage the conduction band at K is seen in the ARPES spectra) and +3 V (lowest voltage the conduction band at $\mathbf{Q}$ is seen in the ARPES spectra). For +3 V, $E_{\mathrm{F}} - E_{\mathrm{C}}$ was found to be 2.4 ± 0.5 meV. As V_{g} is increased, the change in chemical potential is very small when populating the conduction band due to the large density of states and valley degeneracy of the conduction band at $\mathbf{Q}$. E_{F} was found for the gated ARPES spectra by fitting the conduction band at $\mathbf{K}$ with a Gaussian function multiplied by a sigmoid function; see SI Sec. 11.

Section 2: Piezo-force microscopy phase images for device 1 (6° twisted WS_2/WSe_2)

Standard contact-resonant lateral PFM was performed on the heterostructures using a Bruker Dimension Icon AFM with SCM-PIT-V2 cantilevers in a TR probe mount using drive voltage 200-300 mV. Typical contact resonance frequencies were between 650 and 750 kHz. The deflection setpoint is set to saturate the contact resonance amplitude and maintain contact during scanning (usually 0.1V). Coarse topographic mapping for identifying target areas for PFM were done in contact with PFM drive off. The scan surface velocity was <2 µm/s for mapping, and <0.5 µm/s for PFM.

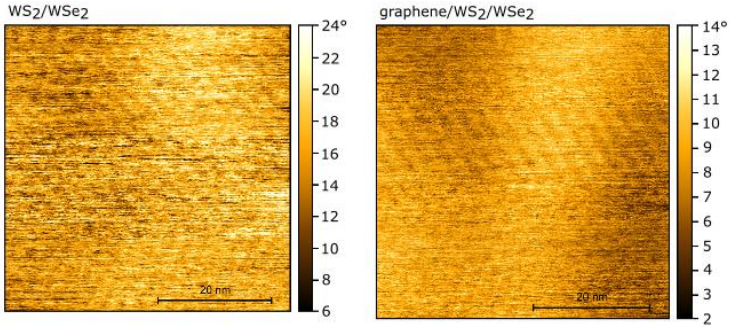

Figure S1: Left – PFM phase of exposed WS_2/WSe_2 region on device 1. Right – PFM phase of graphene-covered WS_2/WSe_2 region. Scale bars, 20 nm. Both images show period/moiré wavelength of ~2.8 nm, which corresponds to a twist angle of ~6° between the WS_2 and WSe_2.

Section 3: Photoluminescence and reflectance measurements to confirm twist angle

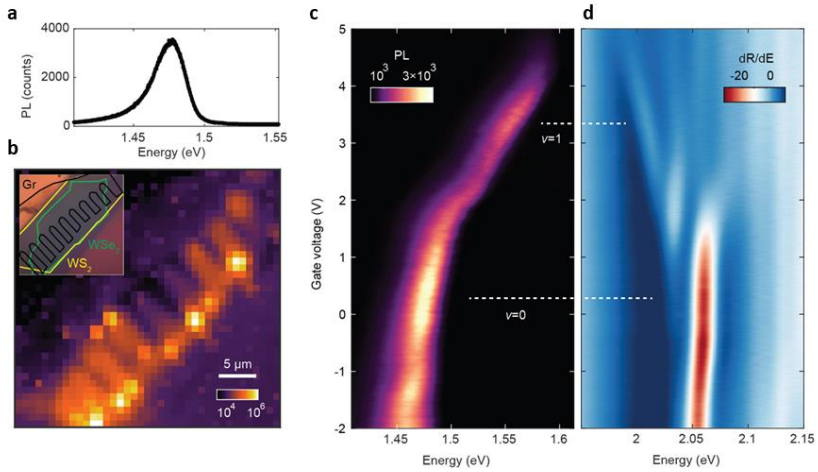

Figure S2: a) Interlayer exciton photoluminescence spectrum at charge neutrality measured at 5 K. The sample was excited using a 1.96 eV laser with a power of 10 µW/µm^2 and the spectra was integrated for 10 seconds. b) Spatial map of integrated photoluminescence intensity, scale bar 5 µm. The heterobilayer region is relatively bright while the region covered by the graphene comb can be distinguished due to suppression in intensity. c) Gate dependent photoluminescence spectra. d) Gate dependence of energy derivative of reflectance contrast spectrum of the WS_2 layer. The filling factor, indicated by white dotted lines, is determined independently through the geometric capacitance, and matches well the kinks in the two spectra.

Section 4: Optical, SPEM and SPIM images at multiple gate voltages

Graphene patterned into a comb shape was used as a top contact to the heterobilayers, as shown in Figure S2a. This reduces the contact resistance in the exposed regions of heterobilayer between the graphene teeth of the comb, reducing drop due to in-plane photocurrent generated by the μARPES beam. In Fig. S2b. are scanning photoemission microscopy (SPEM) images which show the integrated photoemission intensity over a range of energy including E_F and a small range in angle near $\mathbf{\Gamma}$. The regions of high integrated intensity reflect the exposed heterobilayer and complement the graphene comb teeth where the integrated intensity is low and uniform. At V_g = 2 V, the high photoemission intensity near E_F persists only near the comb teeth, reflecting where the conduction band is measurably populated. Simultaneously acquired scanning photoemission current microscopy (SPIM) maps, Fig. S2c., give the photocurrent at each point as the beam is rastered, as measured through the graphene top contact. At V_g = 0 the heterobilayer is insulating, so the photocurrent on it is low and the SPIM image shows high photocurrent only on some of the graphene teeth. The absence of photocurrent from other teeth indicates cracks/gaps in the graphene. At V_g = 1.75 V and above, the SPIM images show uniform photocurrent across the heterobilayer in between the graphene teeth, indicating that it is now conductive. Interestingly, the fingers without photocurrent at low voltages appear in SPIM at 1.5 V, suggesting that they are perhaps being bridged to the main graphene body across narrow cracks via the weakly conducting heterobilayer. Analysis of the photocurrent and band position (extracted from the SPEM images) at a region between the graphene teeth is shown in Figure S2d: the energy of the band position varies linearly with applied gate voltage for V_g < 1.5 V, with correspondingly low photocurrent up to this point. For V_g > 1.5 V the photocurrent increases, and the band energy is no longer linearly related to the gate voltage, consistent with the heterobilayer becoming conducting and effectively grounded with a well-defined Fermi energy.

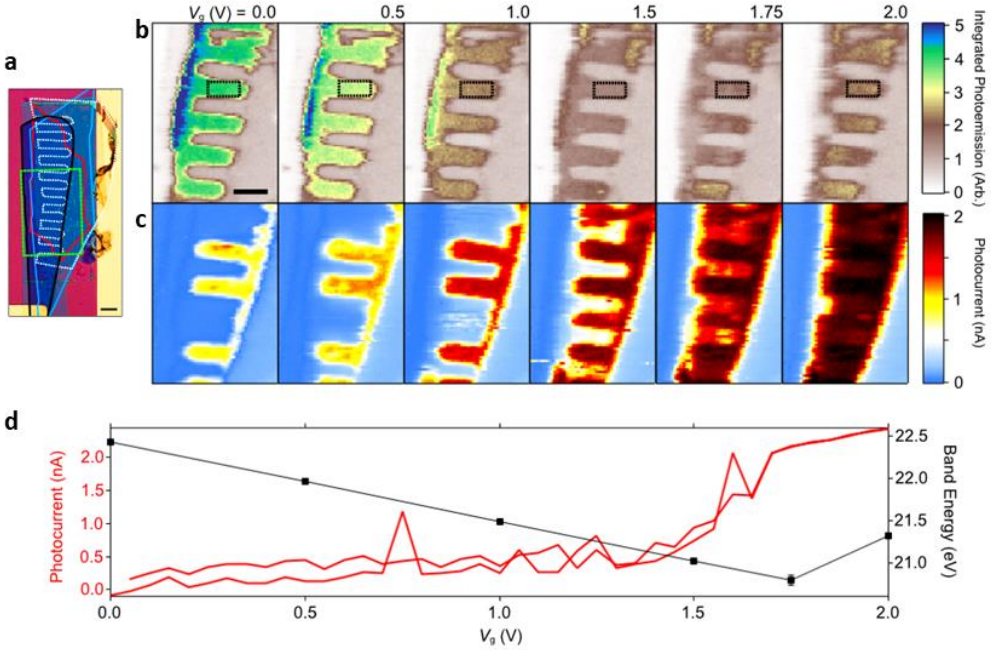

Figure S3: a) Optical image of device 1 outlining WS_2 (blue), WSe_2 (red), cut graphene (dashed white), and graphite (black) regions as transferred. b) SPEM maps (terrain colour scheme) integrated for photoelectron energy E between 20.6 and 24.1 eV with E_F =23.6 eV on a grounded metal electrode and around **Γ**, and c) SPIM maps (cold-hot colour scheme) at multiple gate voltages taken in the area indicated by the yellow dashed box in (a). The bilayer becomes nearly uniformly conducting around 1.75 V. d) Plot of photocurrent (red) and bilayer band position (black) against gate voltage. Band energy found from an average of the black dashed box region in SPEM maps above. All scale bars are 10 μm.

Section 5: Comparison of monolayer and heterobilayer band alignments and band broadening

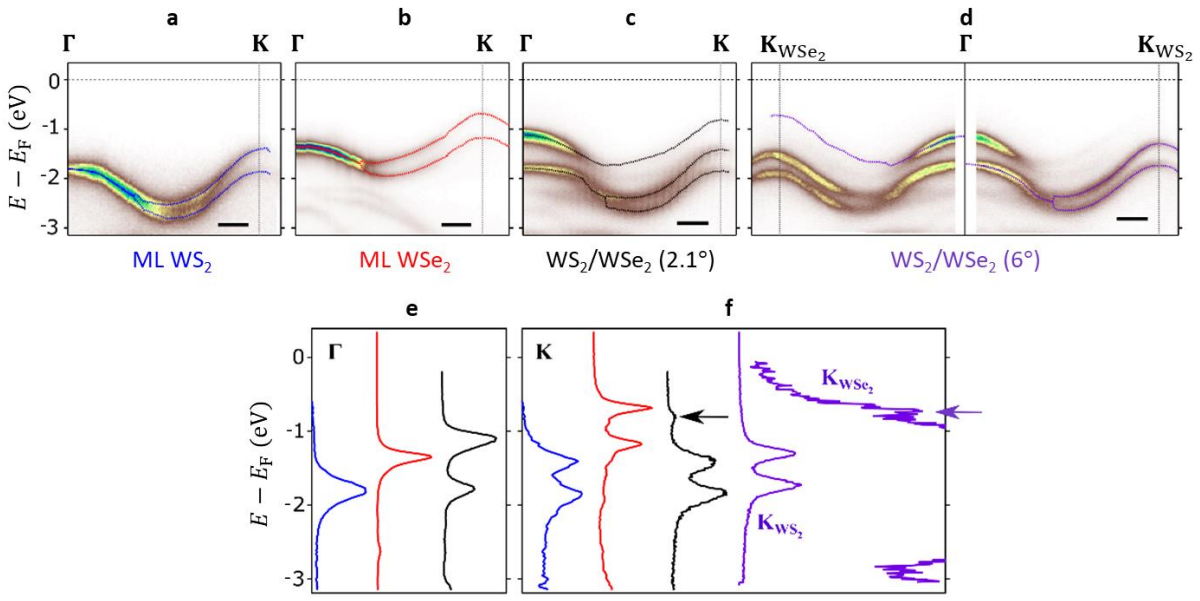

Figure S4: a) and b) μARPES energy-momentum slices along the high symmetry direction for WS_2 and WSe_2 monolayers, respectively. c) and d) μARPES energy-momentum slices along the high symmetry directions defined for the 2° and 6° WS_2/WSe_2 heterobilayers, respectively. Band fits overlaid. Scale bars, 0.2 $Å^{-1}$. e) and f) Energy distribution curves (EDCs) extracted at the high symmetry points, **Γ** and **K,** respectively, from spectra in a-d: ML S_2 (blue), ML WSe_2 (red), 2° WS_2/WSe_2 (black), and 6° WS_2/WSe_2 (purple). Arrows in (f) point to the weak WSe_2 band at **K** for each of the heterobilayers. Band broadenings are of order 0.2 eV (full width at half maximum). Band widths strongly depend on sample quality and annealing temperature prior to measurement.

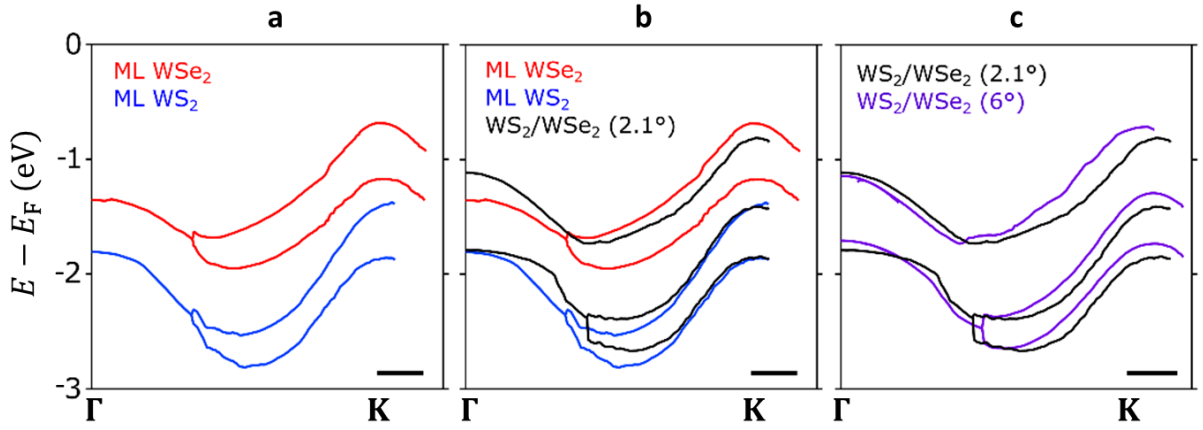

Figure S5: a) Fits of the monolayer WS_2 (blue) and WSe_2 (red) bands from the energy-momentum spectra in Fig. S4. b) Monolayer fits from a) compared to 2° WS_2/WSe_2 heterobilayer band fits (black). WS_2 band structure appears nearly unchanged compared to the monolayer with only a flattening of the band close to **Γ**. Upper band at **Γ** is pushed to lower binding due to hybridisation between the layers. c) Comparison of 2.1° and 6° WS_2/WSe_2 heterobilayer band fits. Small changes in band alignment could be due to a slightly different doping in each sample. Band positions about **Γ** for the 6° heterobilayer are extrapolated due to gap in collected spectra (see Fig. S4d). All fits are also overlaid on the μARPES spectra in Figure S4.

Section 6: Twist angle dependence of WS_2/WSe_2 band structure

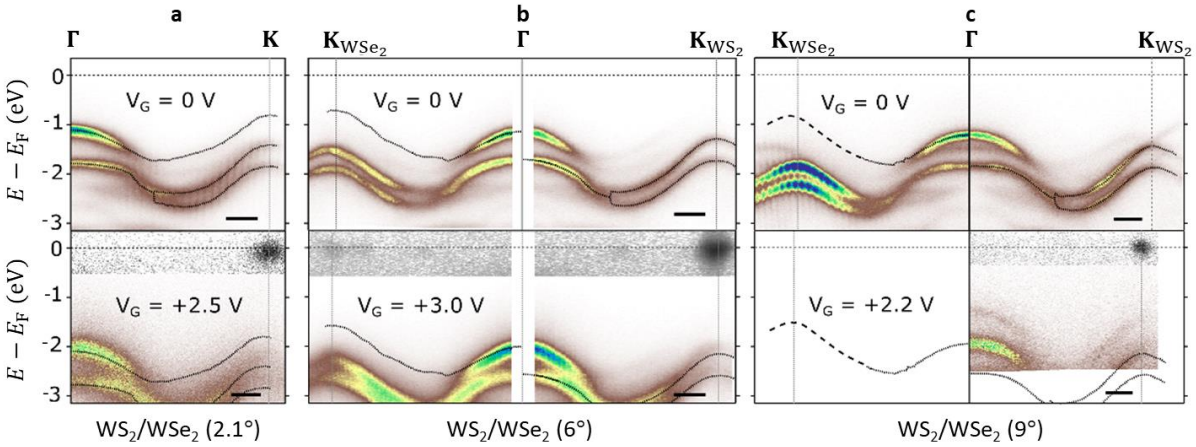

Figure S6: WS_2/WSe_2 band alignments μARPES spectra for three different twist angles: a) 2°, b) 6°, and c) 9°. Dotted lines are fitted band positions. Dashed line is a guide to the eye for the WSe_2 uppermost band at **K**.

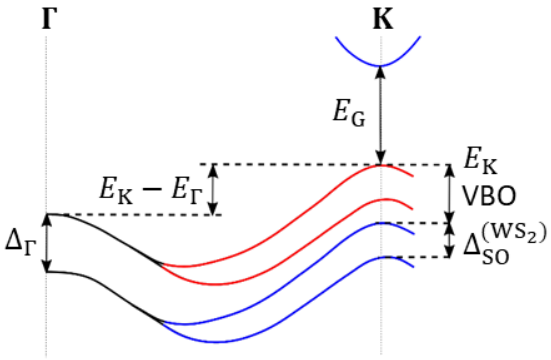

Figure S7: Schematic band diagram for WS_2/WSe_2 heterobilayer. Bands of primarily WSe_2 character, WS_2 character, and of mixed character due to strong interlayer coupling are red, blue and black respectively. Labelled are the binding energies of the local valence band extrema at **Γ** (E_Γ) and **K** (E_K), the energy differences between the valence band edges at the **Γ**-point (Δ_Γ) and at **K** due to spin-orbit coupling in the WS_2 ($\Delta_{SO}^{(WS_2)}$), the energy difference between the WSe_2 and WS_2 valence band edges at **K** (VBO), and the energy difference between the global valence and conduction band extrema (E_G).

Table ST1: WS_2/WSe_2 band alignments for each twist angle with notation for band energies tabulated as defined in Fig. S7. m_K^* is the effective mass at the valence band edge at **K** for WS_2 / WSe_2 respectively. *Uses the energy of the VBM found from the 0 V fit shifted by the electrostatic potential, ΔE_Γ.

*[1] for a carrier concentration of 4.2×10^{12} cm^{-2}. *[2] for a carrier concentration of 6.4×10^{12} cm^{-2}. *[3] for a carrier concentration of 2.4×10^{12} cm^{-2}.

Twist Angle (°)	E_K (eV)	E_Γ - E_K (eV)	$\Delta_{SO}^{(WS2)}$ (eV)	VBO (eV)	Δ_Γ (eV)	$m_K^*(m_0)$	E_G (eV)
2	-0.81 ± 0.03	-0.31 ± 0.04	0.44 ± 0.04	0.60 ± 0.04	0.67 ± 0.04	0.43 ± 0.03 / 0.57 ± 0.05	1.62 ± 0.07*[1]
6	-0.72 ± 0.03	-0.43 ± 0.04	0.44 ± 0.04	0.58 ± 0.04	0.56 ± 0.04	0.38 ± 0.01 / 0.47 ± 0.02	1.58 ± 0.03*[2]
9	-0.92 ± 0.03	-0.30 ± 0.04	0.43 ± 0.04	0.52 ± 0.04	0.61 ± 0.04	0.4 ± 0.1 / not resolved	1.58 ± 0.06*[3]

Section 7: µARPES of WSe_2 on WS_2.

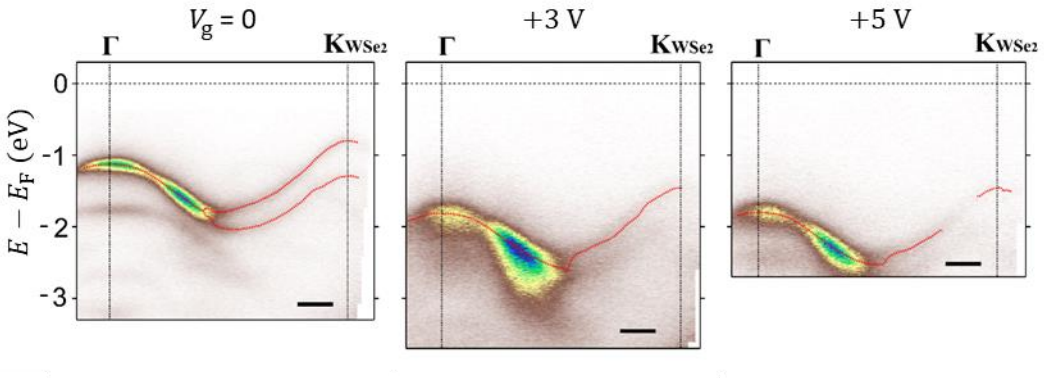

Figure S8: µARPES energy-momentum slices from WSe_2 on WS_2 at gate voltages as shown. The red lines are fits to the upper valence band dispersion, used to find the valence band maximum.

Section 8: Graphene Dirac cone replicas for $WS_2/MoSe_2$ heterobilayer

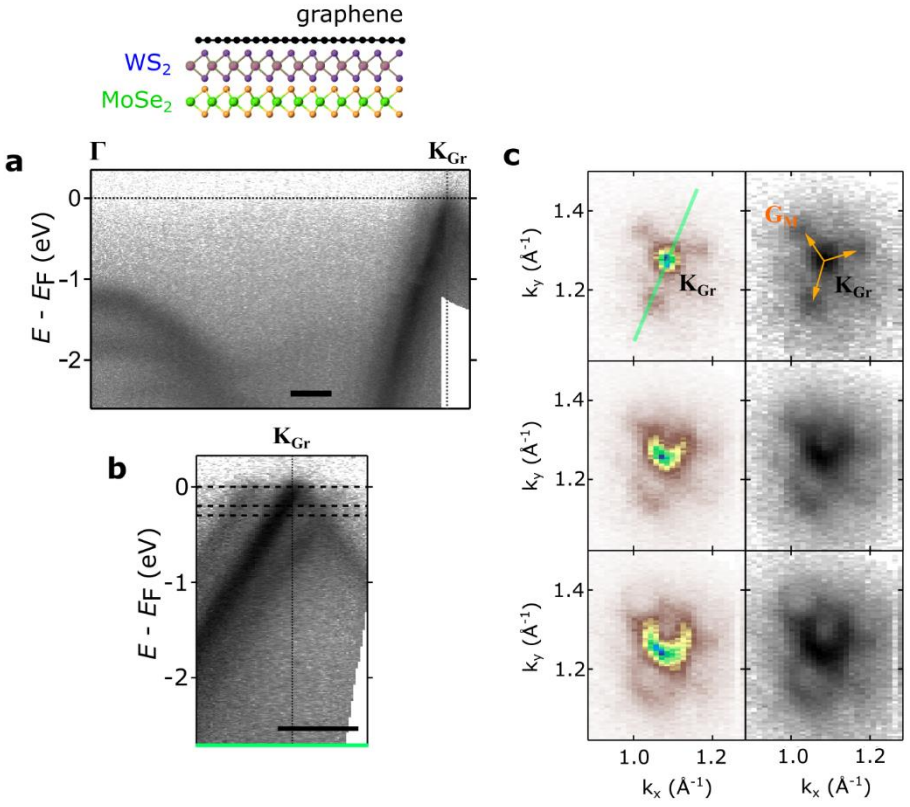

Figure S9: Moiré-replicas in graphene encapsulated $WS_2/MoSe_2$. (a) Energy-momentum slice along Γ-K_{Gr}. Above is schematic of the heterostructure. (b) Higher resolution energy-momentum slice around the graphene Dirac cone, showing two moiré replicas either side of the primary band. Scale bars, 0.2 Å^{-1}. (c) Constant energy maps taken at the energies of the black dashed lines in (b). Green line in top map in (c) shows the position of the energy-momentum slice displayed in (b). Black and white spectra have normalised photoemission intensity displayed in a log scale. Terrain colour scheme shows normalised photoemission intensity in linear scale. Moiré vector, G_M, connecting K_{Gr} and centres of moiré replicas overlaid in orange.

Section 9: WS_2/WSe_2 heterobilayer with 9° twist angle

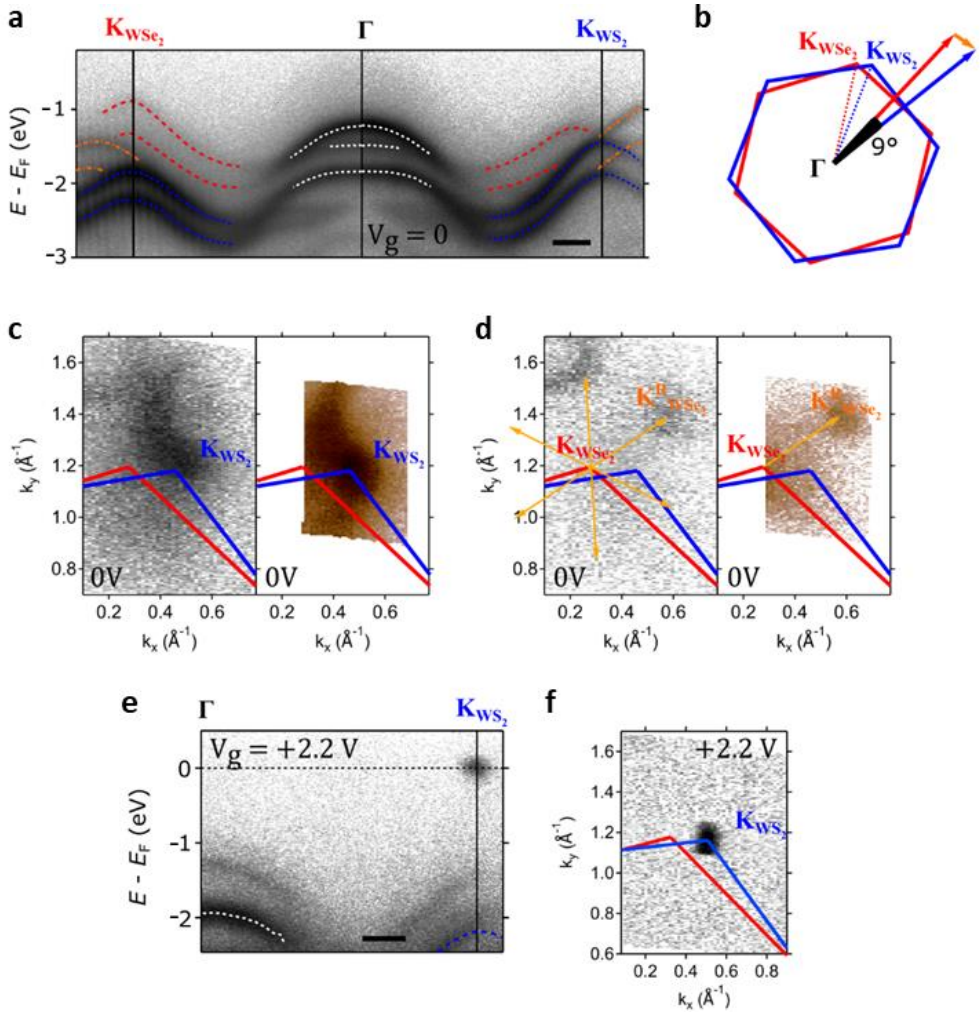

Figure S10: Photoelectron diffraction replica band in WS_2/WSe_2 heterobilayer with 9° twist angle. (a) Energy-momentum slice along the high symmetry directions defined. Overlaid white dotted lines are fits of the bands from the WS_2 layer. Red and orange dashed lines are lines to guide the eye for the bands from the WSe_2 layer and a photoelectron-diffracted WSe_2 band, respectively. Photoemission intensity displayed in log scale. (b) Schematic of the relative orientation of WS_2 and WSe_2 Brillouin zones. (c) and (d) Constant energy maps at the energy of the top of the WS_2 and WSe_2 valence bands, respectively. Map to the right in orange-brown colour scheme is a smaller area higher resolution energy map of the map on the left. Red and blue lines mark the edge of the first Brillouin zone of the WSe_2 and WS_2 layers, respectively. (e) Energy-momentum slice along the high symmetry direction defined at gate voltage of 2.2 V. White and blue dashed lines correspond with bands in (a). (f) Constant energy map at the Fermi energy at a gate voltage of 2.2 V showing no conduction band replicas around the WS_2 conduction band at $\boldsymbol{K}$. Scale bars are 0.2 $Å^{-1}$.

Section 10: Search for valence band replicas in 2° heterobilayer

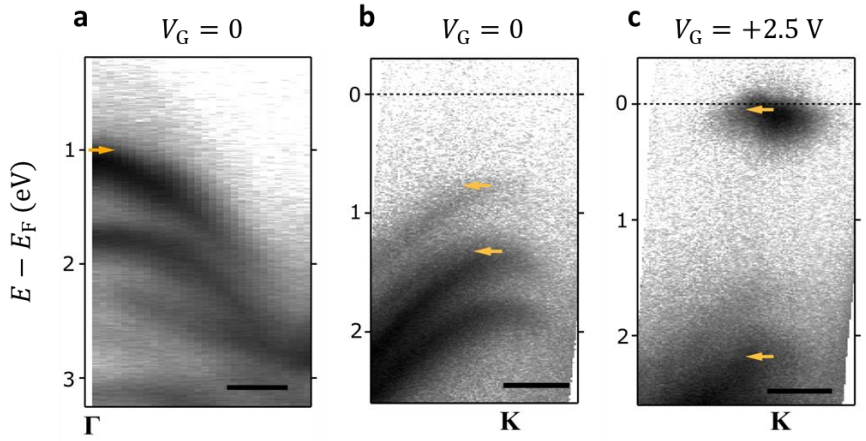

Figure S11: Absence of clearly resolved valence band replicas in device 2. μARPES energy-momentum slice from device 2 around (a) **Γ** and (b) **K** at a gate voltage V_G = 0, and (c) **K** at V_G = +2.5 V. All slices with an averaging of 2 pixels perpendicular to the direction of the slice. Photoemission intensities are displayed in a logarithmic scale. Slices are all taken in direction of one of the moiré vectors, as determined from the graphene replicas. This moiré vector is overlaid as orange arrows on bands of interest at each high symmetry point. Scale bars are 0.2 Å^{-1}.

Section 11: Moiré replica intensities at 2° and 6° twist angle.

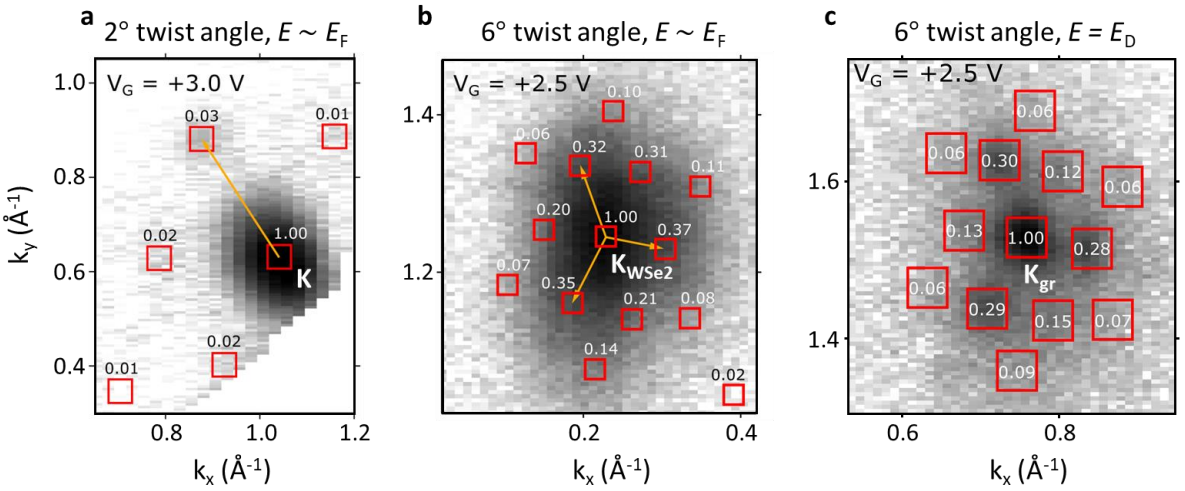

Figure S12: Comparing photoemission intensities around replicas for twist angles of 2° and 6°. μARPES constant energy maps with intensities displayed on logarithmic scale around (a) **K** in device 1 (6°) with V_G = +3V at a binding energy, near E_F, of -0.1 eV averaged over 0.2 eV, (b) $\mathbf{K}_{Wse2}$ (binding energy, near E_F, of -0.1 eV averaged over 0.2 eV) and (c) $\mathbf{K}_{gr}$ (binding energy at Dirac energy E_D = 0.25 eV averaged over 0.1 eV) both in device 2 (2°) with V_G = +2.5V. Small numbers are photoemission intensity integrated within respective red boxes around replica positions, normalized to similarly integrated photoemission of corresponding original band feature. Box positions in (b) are taken from (c) but centered on $\mathbf{K}_{Wse2}$. Boxes are 0.05 Å^{-1} x 0.05 Å^{-1} in (a) and (c), and 0.025 Å^{-1} x 0.025 Å^{-1} in (b). All integrated replica intensities have ~.01 uncertainty so three-fold symmetry in intensity is resolvable in (b) and (c), but not (a).

Section 12: Perturbation theory for the modification of the Bloch states by the moiré potential

In this section, we summarize a calculation for the modification of Bloch states by the moiré potential within first order perturbation theory. We particularly focus on the breaking of six-fold symmetry down to three-fold symmetry in the moiré replica intensities. Due to the fact that the three-fold replica contrast is most prominently displayed in the graphene ARPES spectra in the main text, here we focus on the modifications of the Bloch states in graphene by the moiré scalar and vector potentials. The calculation can be straightforwardly extended to describe the TMD layers.

Consider a single sheet of graphene, in the presence of a C_3 symmetric moiré potential with scalar and vector contributions $U(\boldsymbol{r}) = \sum_{\boldsymbol{G}} U_{\boldsymbol{G}} e^{i\boldsymbol{G}\cdot\boldsymbol{r}}$ and $\boldsymbol{A}(\boldsymbol{r}) = \sum_{\boldsymbol{G}} \boldsymbol{A}_{\boldsymbol{G}} e^{i\boldsymbol{G}\cdot\boldsymbol{r}}$, respectively, where $\{\boldsymbol{G}\}$ are the reciprocal lattice vectors of the moiré superlattice (see main text). Due to the fact that the moiré potentials are real-valued, their Fourier components satisfy $U_{-\boldsymbol{G}} = U_{\boldsymbol{G}}^*$ and $\boldsymbol{A}_{-\boldsymbol{G}} = \boldsymbol{A}_{\boldsymbol{G}}^*$. Under a C_3 rotation O of the moiré reciprocal lattice vector, $\boldsymbol{G} \to O\boldsymbol{G}$, the moiré potential components transform as $U_{O\boldsymbol{G}} = U_{\boldsymbol{G}}$ and $\boldsymbol{A}_{O\boldsymbol{G}} = O\boldsymbol{A}_{\boldsymbol{G}}$. These transformation properties, which follow from the C_3 symmetry of the moiré potential, will be important below when we assess the symmetry properties of the moiré replicas in the perturbed wave function.

Focusing on states near valley K, we write the single particle Hamiltonian as $\widehat{H} = \widehat{H}_0 + \widehat{V}$, with $\widehat{H}_0 = v\,\hat{\boldsymbol{p}}\cdot\boldsymbol{\sigma}$ and $\widehat{V} = U(\hat{\boldsymbol{r}}) + v\boldsymbol{A}(\hat{\boldsymbol{r}})\cdot\boldsymbol{\sigma}$, where v is the Dirac velocity, $\boldsymbol{\sigma}$ is a vector of Pauli matrices acting on the pseudospin (AB sublattice) space, and we have set $|e| = 1$, where $e < 0$ is the electron charge. For convenience below, we write $\widehat{V} = \sum_{\boldsymbol{G}} V_{\boldsymbol{G}} e^{i\boldsymbol{G}\cdot\hat{\boldsymbol{r}}}$, where $V_{\boldsymbol{G}} = U_{\boldsymbol{G}} + v\boldsymbol{A}_{\boldsymbol{G}}\cdot\boldsymbol{\sigma}$. In the absence of the moiré perturbation, the graphene Bloch band eigenstate in band n (labelling the conduction and valence bands) and at crystal momentum $\boldsymbol{k}$ (measured relative to the Dirac point) is described by

$$\widehat{H}_0|\psi_{n\boldsymbol{k}}^{(0)}\rangle = \varepsilon_{n\boldsymbol{k}}^{(0)}|\psi_{n\boldsymbol{k}}^{(0)}\rangle,\ \ |\psi_{n\boldsymbol{k}}^{(0)}\rangle = e^{i\boldsymbol{k}\cdot\hat{\boldsymbol{r}}}\,|u_{n\boldsymbol{k}}^{(0)}\rangle,$$

where $\left|u_{n\boldsymbol{k}}^{(0)}\right\rangle$ is the periodic Bloch function and $\varepsilon_{n\boldsymbol{k}}^{(0)} = \pm\hbar v|\boldsymbol{k}|$ is the corresponding unperturbed energy, with + and – corresponding to the conduction and valence bands, respectively.

We now seek the perturbed wave function $|\psi_{n\boldsymbol{k}}\rangle = |\psi_{n\boldsymbol{k}}^{(0)}\rangle + |\psi_{n\boldsymbol{k}}^{(1)}\rangle + \cdots$, modified by the presence of the moiré potential. Following a few lines of algebra, the correction to the wave function to first order in the perturbation, denoted $\left|\psi_{n\boldsymbol{k}}^{(1)}\right\rangle$, can be written as

$$|\psi_{n\boldsymbol{k}}^{(1)}\rangle = \sum_{m\boldsymbol{G}} |\psi_{m,\boldsymbol{k}+\boldsymbol{G}}^{(0)}\rangle\langle\langle u_{m,\boldsymbol{k}+\boldsymbol{G}}^{(0)}|\frac{1}{\varepsilon_{n\boldsymbol{k}}^{(0)} - \widetilde{H}_{\boldsymbol{k}+\boldsymbol{G}}} V_{\boldsymbol{G}}|u_{n\boldsymbol{k}}^{(0)}\rangle\rangle,$$

where $|u_{n\boldsymbol{k}}^{(0)}\rangle\rangle$ is the periodic Bloch function restricted to one unit cell, and $\widetilde{H}_{\boldsymbol{k}}$ is the Bloch Hamiltonian $\widehat{H}_{\boldsymbol{k}} = e^{-i\boldsymbol{k}\cdot\hat{\boldsymbol{r}}}\widehat{H}e^{i\boldsymbol{k}\cdot\hat{\boldsymbol{r}}}$ restricted to one unit cell. In the two-band tight-binding description, and ignoring spin, $\widetilde{H}_{\boldsymbol{k}}$ is a 2×2 matrix acting on the pseudospin degree of freedom.

Using the first-order corrections to the wave functions written above, we define the probability associated with the moiré sideband of the state $|\psi_{n\boldsymbol{k}}\rangle$ at crystal momentum $\boldsymbol{k}+\boldsymbol{G}$, summed over the conduction and valence bands, as

$$P_{\boldsymbol{k}+\boldsymbol{G}} = \sum_m |\langle\langle u_{m,\boldsymbol{k}+\boldsymbol{G}}^{(0)}|\frac{1}{\varepsilon_{n\boldsymbol{k}}^{(0)} - \widetilde{H}_{\boldsymbol{k}+\boldsymbol{G}}} V_{\boldsymbol{G}}|u_{n,\boldsymbol{k}}^{(0)}\rangle\rangle|^2 = \langle\langle u_{n\boldsymbol{k}}^{(0)}|V_{\boldsymbol{G}}^{\dagger}\frac{\varepsilon_{n\boldsymbol{k}}^{(0)} + \hbar v(\boldsymbol{k}+\boldsymbol{G})\cdot\boldsymbol{\sigma}}{\left(\left[\varepsilon_{n\boldsymbol{k}}^{(0)}\right]^2 - |\hbar v(\boldsymbol{k}+\boldsymbol{G})|^2\right)^2} V_{\boldsymbol{G}}|u_{n\boldsymbol{k}}^{(0)}\rangle\rangle.$$

To evaluate the moiré replica intensity $P_{\boldsymbol{k}+\boldsymbol{G}}$ we use $V_{\boldsymbol{G}} = U_{\boldsymbol{G}} + v\boldsymbol{A}_{\boldsymbol{G}}\cdot\boldsymbol{\sigma}$, along with the identity $(\boldsymbol{a}\cdot\boldsymbol{\sigma})(\boldsymbol{b}\cdot\boldsymbol{\sigma}) = \boldsymbol{a}\cdot\boldsymbol{b} + i(\boldsymbol{a}\times\boldsymbol{b})\cdot\boldsymbol{\sigma}$. We furthermore use the fact that the pseudospins associated with the graphene Bloch

band eigenstates are oriented within the equatorial plane of the Bloch sphere: $\left\langle\left\langle u_{n\boldsymbol{k}}^{(0)}|(\boldsymbol{z}\cdot\boldsymbol{\sigma})|u_{n\boldsymbol{k}}^{(0)}\right\rangle\right\rangle = 0$. Working in the regime $|\boldsymbol{k}| \ll |\boldsymbol{G}|$, after several lines of algebra we obtain the leading contributions in $|\boldsymbol{k}|/|\boldsymbol{G}|$:

$$P_{\boldsymbol{k}+\boldsymbol{G}} = \frac{|\hbar v\boldsymbol{G}|^2 - 2(\hbar v)^2\boldsymbol{k}\cdot\boldsymbol{G}}{|\hbar v\boldsymbol{G}|^4}[U_{\boldsymbol{G}}^* U_{\boldsymbol{G}} + v^2\boldsymbol{A}_{\boldsymbol{G}}^*\cdot\boldsymbol{A}_{\boldsymbol{G}} + v(U_{\boldsymbol{G}}^*\boldsymbol{A}_{\boldsymbol{G}} + U_{\boldsymbol{G}}\boldsymbol{A}_{\boldsymbol{G}}^*)\cdot\langle\langle\boldsymbol{\sigma}\rangle\rangle]$$
$$+\frac{2\hbar v\,\varepsilon_{n\boldsymbol{k}}^{(0)}}{|\hbar v\boldsymbol{G}|^4}\{vU_{\boldsymbol{G}}^*(\boldsymbol{G}\cdot\boldsymbol{A}_{\boldsymbol{G}}) + vU_{\boldsymbol{G}}(\boldsymbol{G}\cdot\boldsymbol{A}_{\boldsymbol{G}}^*) + [v^2(\boldsymbol{G}\cdot\boldsymbol{A}_{\boldsymbol{G}})\boldsymbol{A}_{\boldsymbol{G}}^* + v^2(\boldsymbol{G}\cdot\boldsymbol{A}_{\boldsymbol{G}}^*)\boldsymbol{A}_{\boldsymbol{G}} + (U_{\boldsymbol{G}}^*U_{\boldsymbol{G}} - v^2\boldsymbol{A}_{\boldsymbol{G}}^*\cdot\boldsymbol{A}_{\boldsymbol{G}})\boldsymbol{G}]\cdot\langle\langle\boldsymbol{\sigma}\rangle\rangle\},$$

where we have introduced the shorthand $\langle\langle\boldsymbol{\sigma}\rangle\rangle = \langle\langle u_{n\boldsymbol{k}}^{(0)}|\boldsymbol{\sigma}|u_{n\boldsymbol{k}}^{(0)}\rangle\rangle$. Importantly, in the unperturbed eigenstates, the pseudo spin expectation value is oriented along the direction of $\boldsymbol{k}$: $\langle\langle\boldsymbol{\sigma}\rangle\rangle \propto \boldsymbol{k}$.

According to the symmetry properties outlined above, all terms in the expression for $P_{\boldsymbol{k}+\boldsymbol{G}}$ are invariant under simultaneous 120° rotations of $\boldsymbol{k}$ and $\boldsymbol{G}$, as required by C_3 symmetry. To characterize the relative contrast of moiré replicas shifted by the moiré reciprocal lattice vectors $\boldsymbol{G}_{\pm1,\pm2,\pm3}$, we average $P_{\boldsymbol{k}+\boldsymbol{G}}$ over the direction of $\boldsymbol{k}$, for fixed $|\boldsymbol{k}| = k_F$ at the unperturbed Fermi surface: $\bar{P}_{\boldsymbol{G}} = \oint d\theta_{\boldsymbol{k}}\, P_{\boldsymbol{k}+\boldsymbol{G}}$, with $\boldsymbol{k} = k_F(\cos\theta_{\boldsymbol{k}}, \sin\theta_{\boldsymbol{k}})$. After this averaging we obtain

$$\bar{P}_{\boldsymbol{G}} = \frac{1}{|\hbar v\boldsymbol{G}|^2}[U_{\boldsymbol{G}}^*U_{\boldsymbol{G}} + v^2\boldsymbol{A}_{\boldsymbol{G}}^*\cdot\boldsymbol{A}_{\boldsymbol{G}}] + \frac{\hbar v k_F}{|\hbar v\boldsymbol{G}|^4}(\hbar v\boldsymbol{G})\cdot v(U_{\boldsymbol{G}}^*\boldsymbol{A}_{\boldsymbol{G}} + U_{\boldsymbol{G}}\boldsymbol{A}_{\boldsymbol{G}}^*).$$

The first term above is invariant under $\boldsymbol{G}\to-\boldsymbol{G}$, and thus gives a six-fold symmetric contribution to the replica intensity. The second term is *odd* under $\boldsymbol{G}\to-\boldsymbol{G}$. Thus we see that while $\bar{P}_{\boldsymbol{G}}$ is invariant under 120° rotations of $\boldsymbol{G}$, i.e., $\bar{P}_{\boldsymbol{G}_1} = \bar{P}_{\boldsymbol{G}_2} = \bar{P}_{\boldsymbol{G}_3}$ (see main text for definitions of $\boldsymbol{G}_{1,2,3}$, the replica probabilities are *not* invariant under 180° (equivalently, 60°) rotations: $\bar{P}_{\boldsymbol{G}_1} \neq \bar{P}_{\boldsymbol{G}_{-1}}$, etc.

Section 13: Determining band shifts, carrier concentrations, photocurrent, and the conduction band minimum

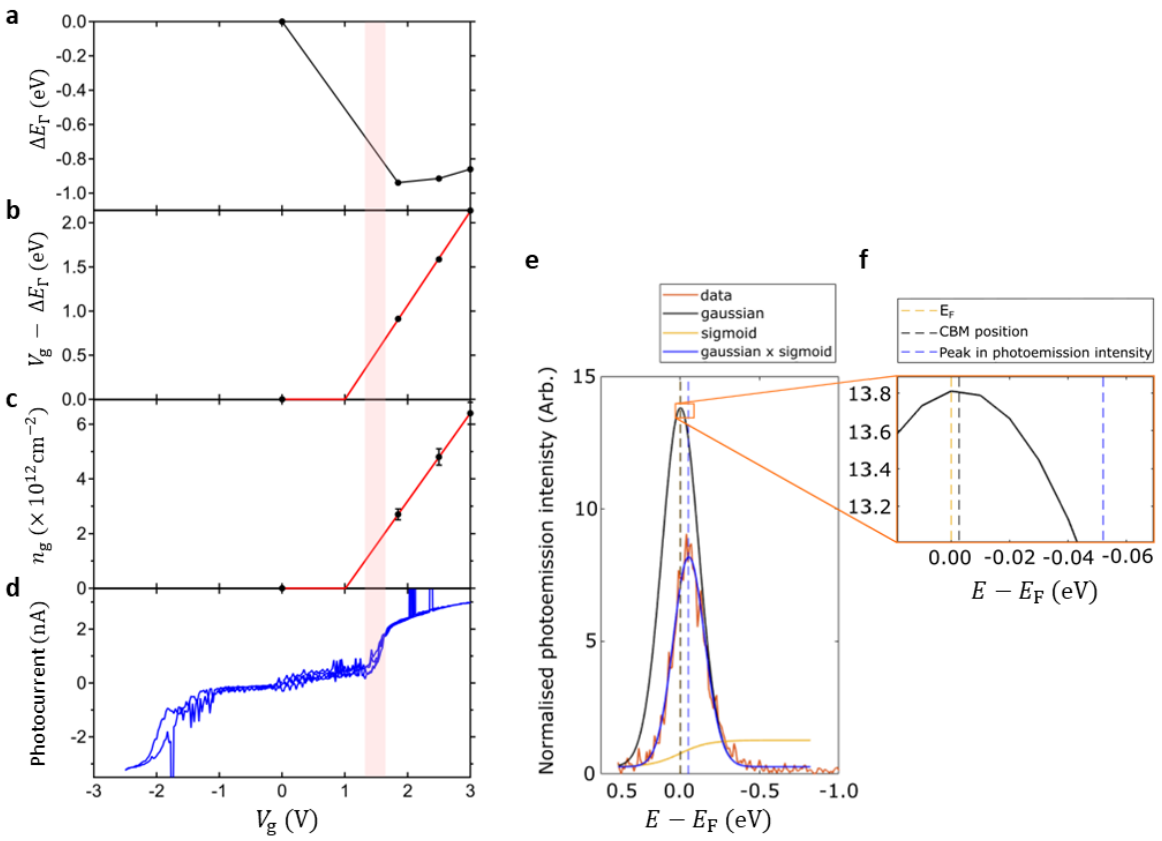

Figure S13: Gate induced band shifts and photocurrent in WS_2/WSe_2 heterobilayer with 6° twist angle. Gate voltage V_g dependence of a) Electrostatic shift of the bands, ΔE_Γ; b) Effective potential, V_G - ΔE_Γ; c) Carrier concentration, n_g; and d) Photocurrent from gate to ground electrode. Pink strip indicates the region where the heterobilayer becomes conducting. e) CBM fit for central EDC shown in Figure 1h. f) zoomed-in region highlighted in orange in e) shows the positions in binding of the CBM and the peak in photoemission intensity relative to the Fermi energy, E_F. Peak in photoemission intensity, E-E_F = -0.052 ± 0.003 eV. CBM position = -0.006 ± 0.003 eV. The same Sigmoid function was used in all the EDC fits shown in Figure 1h.

References

(1) Nguyen, P. V.; Teutsch, N. C.; Wilson, N. P.; Kahn, J.; Xia, X.; Graham, A. J.; Kandyba, V.; Giampietri, A.; Barinov, A.; Constantinescu, G. C.; Yeung, N.; Hine, N. D. M.; Xu, X.; Cobden, D. H.; Wilson, N. R. Visualizing Electrostatic Gating Effects in Two-Dimensional Heterostructures. *Nature* **2019**, *572* (7768), 220–223. https://doi.org/10.1038/s41586-019-1402-1.

(2) Dudin, P.; Lacovig, P.; Fava, C.; Nicolini, E.; Bianco, A.; Cautero, G.; Barinov, A. Angle-Resolved Photoemission Spectroscopy and Imaging with a Submicrometre Probe at the SPECTROMICROSCOPY-3.2L Beamline of Elettra. *J. Synchrotron Radiat.* **2010**, *17* (4), 445–450. https://doi.org/10.1107/S0909049510013993.